



Three-dimensional CTF correction improves the resolution of electron tomograms



Michael Kunz, Achilleas S. Frangakis*

Goethe University Frankfurt, Buchmann Institute for Molecular Life Sciences and Institute for Biophysics, Max-von-Laue Str. 15, 60438 Frankfurt am Main, Germany

ARTICLE INFO

Article history:

Received 4 April 2016

Received in revised form 20 June 2016

Accepted 21 June 2016

Available online 23 June 2016

Keywords:

CTF correction

Electron tomography

Image processing

ABSTRACT

Correction of the contrast transfer function (CTF) of the microscope is a necessary step, in order to achieve high resolution from averaged electron microscopic images. Thereby, the CTF is first estimated and subsequently the electron micrograph is corrected, so that the negative oscillations of the CTF are equalized. Typically, the CTF correction is performed in 2D and the tilt-induced focus gradient is taken into account. Most often, the sample-thickness-induced focus gradient is ignored. Theoretical considerations, as well as implementation suggestions, for a 3D CTF correction that considers both gradients have been proposed before, although an implementation achieving a resolution improvement has been lacking, primarily due to computational reasons. Here, we present a comprehensive solution for a 3D CTF correction based on the Jensen-Kornberg scheme, which performs a slice-by-slice correction of the CTF within the tomographic reconstruction. We show that the computational requirements are comparable to those of 2D CTF correction. Using the examples of mitochondrial ribosomes and tobacco mosaic virus we demonstrate the improvement of the reconstruction quality with the 3D CTF correction, and the resolution gain on sub-tomogram averaging. More interestingly, for tomographic applications, the quality of the individual sub-tomograms before averaging increases significantly. We find that 3D CTF correction always produces equal or better results than 2D CTF correction.

© 2016 Elsevier Inc. All rights reserved.

1. Introduction

Electron micrographs are affected by the contrast transfer function (CTF) of the microscope. Modern sub-tomogram averaging procedures that achieve a resolution far beyond the first zero crossing of the CTF require CTF-corrected tilt-series. To date, several CTF-correction methods have been presented; they can be categorized into three principal approaches: (a) Two-dimensional (2D) CTF correction of electron micrographs based on the patch-based approach to compensate for the tilt-induced focus gradient (Fernández et al., 2006; Zanetti et al., 2009; Xiong et al., 2009), (b) CTF correction coupled with sub-tomogram averaging (Bharat et al., 2015), and (c) a complete three-dimensional (3D) CTF correction, which can compensate for the tilt-induced and the sample-thickness-induced focus gradient (Jensen and Kornberg, 2000). The first two approaches, while they are currently the most applicable, have distinct limitations. 2D CTF correction in patches on the micrograph prior to the tomographic reconstruction (referred to as the reconstruction from here on) results in an entirely

CTF-corrected reconstruction; however, the focus variation due to the sample thickness cannot be corrected. CTF correction of sub-tomograms allows to compensate for focus variations due to sample thickness, however only the individual sub-tomograms are finally CTF corrected and not the entire tomographic reconstruction, thus it relies on the multiple occurrence of the object of interest (Schur et al., 2013; Pfeffer et al., 2015b; Bharat et al., 2015). Conceptually, the most complete approach was proposed by Jensen and Kornberg (Jensen and Kornberg, 2000), which performed a truly 3D CTF correction for the tilt-induced and sample-thickness-induced focus gradient in the tilt-series. While the mathematical justification has been provided later (Kazantsev et al., 2010), a feasible implementation was still missing. A reliable 3D CTF correction with a proper reconstruction technique could hold the promise of reaching a level of quality that would allow for the detection of individual macromolecular complexes in the cellular context without the need for sub-tomogram averaging.

A 3D CTF correction that incorporates both the tilt-induced and the sample-thickness-induced focus gradients within the reconstruction requires that individual planes perpendicular to the beam direction (which we call “slices”) are corrected according to the focus they were imaged. Previously, it was shown mathematically

* Corresponding author.

E-mail address: achilleas.frangakis@biophysik.org (A.S. Frangakis).

that this can lead to an accurately CTF-corrected reconstruction (Kazantsev et al., 2010). Current computational solutions in Fourier space, even based on algorithmic simplifications (Voortman et al., 2011), are computationally so expensive, that render a practicable reconstruction difficult. Currently, the only practical CTF-corrected non-downsampled reconstruction, must be carried out in 2D by segmenting the micrographs into patches along the tilt axis chosen such that they have an approximately constant defocus value (Fernández et al., 2006; Xiong et al., 2009). These patches are then independently CTF-corrected either by simple phase flipping the spatial frequencies with a negative CTF, or by using more advanced correction schemes like Wiener filtering that also accommodates for the sine-like characteristic and the dampening envelope of the CTF. Nevertheless, to incorporate the sample-thickness-induced focus gradient along the beam direction, the CTF correction must be carried out in 3D on the reconstruction and not on the 2D electron micrographs.

Here we present a very fast 3D CTF correction approach based on the Jensen-Kornberg scheme (Jensen and Kornberg, 2000) that incorporates both focus gradients within the tomographic reconstruction procedure, and can deliver a tomographic reconstruction with a complete 3D CTF correction. We implemented two reconstruction methods: weighted back-projection and the super-sampling simultaneous algebraic reconstruction techniques (SART) (Kunz and Frangakis, 2014), that can be used with the 3D CTF correction at only slightly slower reconstruction speeds. We show that a 4 K reconstruction can be calculated in just over 7 min, and a 2 K reconstruction within 2 min on a conventional GPU, which is only a few additional minutes compared to the non-CTF-corrected reconstruction.

2. Material and methods

2.1. CTF determination

The CTF describes the modulation of the spatial frequencies (f) of the imaged sample as a function of various microscope parameters. It can be written as:

$$CTF(f) = A \left(\sin \left(\pi \lambda f^2 (\Delta z - 0.5 \lambda^2 f^2 C_s) \right) + B \cos \left(\pi \lambda f^2 (\Delta z - 0.5 \lambda^2 f^2 C_s) \right) \right) \quad (\text{Erickson and Klug, 1971; Wade, 1992}).$$

The defocus is denoted as Δz , the electron wavelength as λ and the spherical aberration constant of the objective lens as C_s . A is an envelope function to represent the dampening of higher frequencies, often approximated by a simple Gaussian decay. B denotes the ratio of phase to amplitude contrast, which for cryo-EM images is usually approximated by the value 0.1.

The CTF-determination for a 3D CTF-correction requires the estimation of two main parameters: (a) the estimation of the defocus value, and (b) The estimation of the defocus contribution to the CTF of individual features depending of their placement in the reconstruction. While the estimation of the defocus in the image is a common task, estimating the CTF contributions depending on their beam placement in the reconstruction is more challenging. Several methods have been suggested for estimating the CTF on an image (Marabini et al., 2015). Here we use FASTDEF (Vargas et al., 2013), which can determine multiple CTF parameters such as defocus and astigmatism at very low dose conditions. It is often the case that only a few Thon rings are visible in the power spectra calculated from the individual projection images in the cryo tilt-series, especially for the images recorded at high tilt angles. Advantageously, it is also possible to estimate a noise and background term in the measured power spectrum using FASTDEF. This background term can also be used as a normalization function. When dividing the power spectrum of the original micrograph by this background term one obtains a well normalized power

spectrum with values in the range between minus one and one. We explore this normalized power spectrum for estimating the CTF at the higher tilt angles.

2.2. Data recording parameters of the mitochondrial ribosomes and tobacco mosaic virus

Two data sets were used to demonstrate the performance of the 3D CTF correction. (a) Reconstructions of mitochondrial ribosomes (Pfeffer et al., 2015a), and (b) The tobacco mosaic virus (TMV). For the mitochondrial reconstruction the recording parameters are described in detail elsewhere (Pfeffer et al., 2015a). The TMV tilt-series were recorded on a FEI 300 kV Titan Krios TEM (FEI, Eindhoven, Netherlands) with a K2 direct detector (Gatan, Pleasanton, USA) at 64.000 \times magnification and a nominal pixel-size of 1.1 Å, with the camera operating in super-resolution mode (8 k \times 8 k images) and using dose fractionation mode with four frames and a total exposure time of 2 s. The tilt-range was between -60° and 60° with three degrees increment and a commutative electron dose accumulated of 80 e⁻/Å². The measured defocus across the tilt-series varied around 2 μ m. The defocus of each micrograph was estimated by various methods (including IMOD), and in all cases they provided similar results. For the comparison of the CTF correction schemes thicker areas with overlapping viruses were chosen with a thickness of \sim 150 nm.

2.3. The principle and implementation of 3D CTF correction

When the entire electron micrograph has the same defocus as in the case of a projection of a very thin untilted sample, a CTF correction can be applied on the entire electron micrograph. When the sample is tilted within the microscope, the focus varies perpendicular to the tilt axis. If the sample is considerably thick, a focus variation within the sample is also present. During cryo-electron tomography the sample thus experiences two focus gradients: one gradient due to the tilt, and a second gradient due to the sample thickness. In tomography both effects get more pronounced at higher tilt angles (Fig. 1).

For the 3D CTF correction, the tomographic reconstruction undergoes the inverse process that the sample experienced during recording. Thereby, the reconstruction is placed within the volume and is tilted according to the tilt angle such that the projection along the electron beam direction results in the same view as the corresponding micrograph. The reconstruction is then sliced perpendicular to the beam direction and each slice is CTF corrected. The thickness of the slice can be chosen according to the computational needs, and can vary from one voxel to the complete thickness of the sample; the later renders it equivalent to the image patches based CTF correction. Importantly, the coordinate system used here is the same as that of the microscope (Kazantsev et al., 2010). After determining a feature e.g. a specific object with high contrast, or a patch of the carbon support film for which the defocus value Δz can be precisely measured, the correction of the CTF, only depends on the positioning of the reconstruction in the beam direction (Fig. 2). This determining feature acts as a defocus fiducial, and is being used as a reference point for the whole 3D CTF correction. Subsequently, each slice is then subjected to CTF correction according to its beam position relative to the determining feature (the defocus fiducial). Increasing or decreasing defocus values are used, when moving up or down in the volume respectively. In doing so, not only is a focus variation due to the tilted object incorporated, but the sample-thickness-induced focus gradient is also explicitly dealt with. Thus, the CTF correction is no longer performed on the micrograph itself, but on every slice of the reconstruction (Fig. 2).

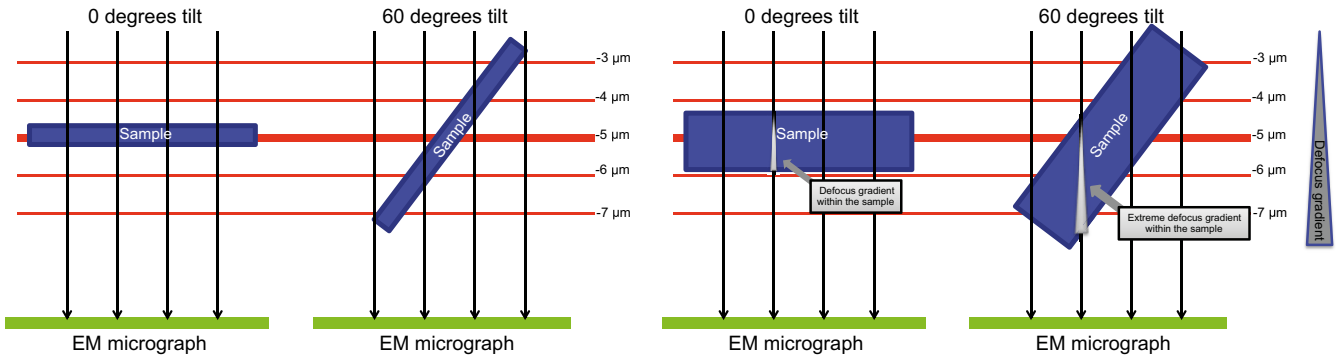


Fig. 1. In thin samples the only focus gradient that usually matters is the gradient due to sample tilting during tilt-series acquisition. As soon as the sample reaches a certain thickness, which is often the case in cryo-electron tomography of whole cells, the focus gradient along the direction of projection becomes a more important factor. This sample-thickness-induced gradient increases, when the sample is tilted.

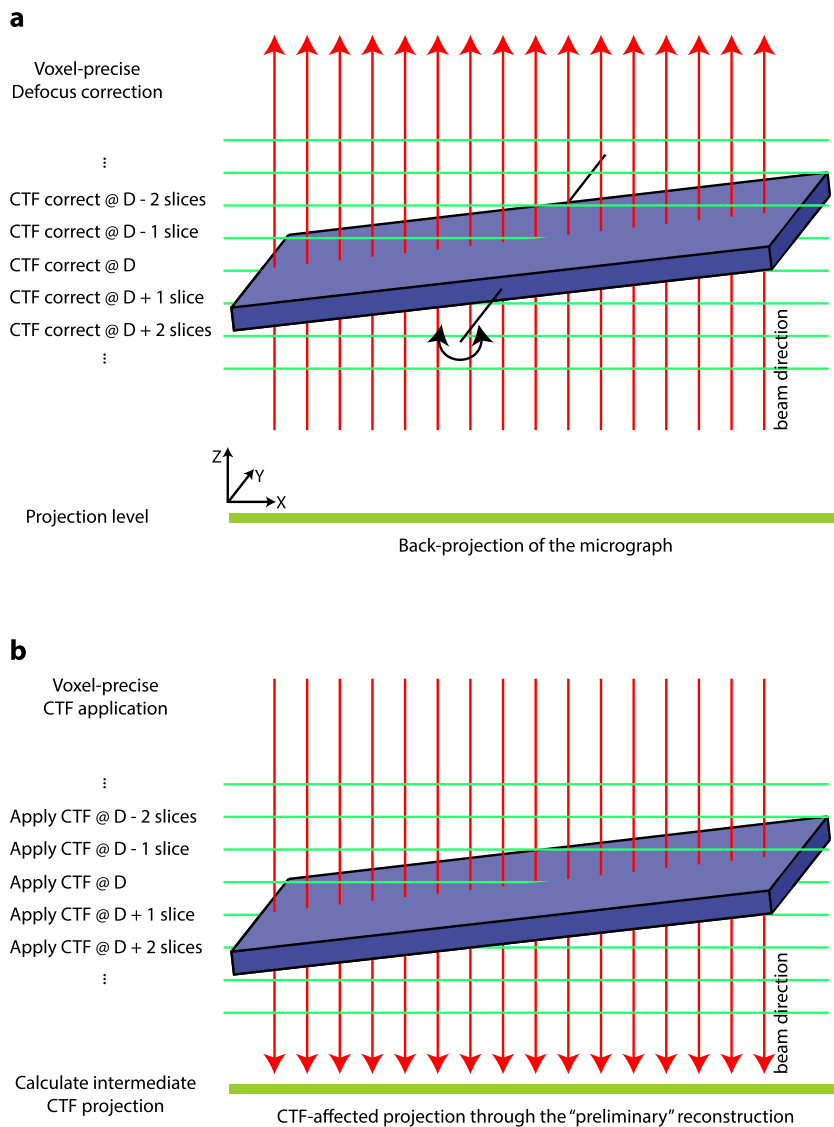


Fig. 2. Volume slicing and coordinate system used: (a) For the back-projection the reconstruction is sliced perpendicular to the beam direction. Each slice is independently CTF corrected by Wiener filtering. (b) For the forward-projection that is only necessary for SART, a CTF-affected projection has to be obtained from the CTF-corrected intermediate reconstruction. The microscope process is simulated by slicing the reconstruction perpendicular to the beam direction. Before summing up the individual slices, the CTF is imposed on each slice by phase-flipping the corresponding CTF components.

Many algorithms treat the reconstruction as a rigid 3D image, and interpolate the individual electron micrographs of the tilt-series so that they match the reconstruction Cartesian voxel arrangement. This interpolation happens as a result of the alignment of the tilt-series, while compensating for all affine transformations and image distortions. Similarly, the micrographs are also interpolated when corrected for the CTF. Here, with the coordinate system introduced before, the tomographic reconstruction experiences all the affine transformations as well as CTF correction so that its projection along the beam direction matches the recorded micrograph (Kazantsev et al., 2010). Importantly, all interpolations are only applied on the tomographic reconstruction. The tomographic reconstruction is placed into the appropriate position defined by rotating, tilting and warping functions, as well as shifting up or down in the beam direction in order to match the proper defocus settings. In this way the original micrograph is never modified.

In this implementation, the performance gain of the 3D CTF correction and its practical implementation is demonstrated with super-sampling SART and weighted back-projection (WBP). Whereas the WBP implementation directly follows the Jensen-Kornberg approach, the super-sampling SART method requires some adaptations. With SART being a member of the algebraic reconstruction technique family, the reconstruction is calculated by a sequence of forward- and back-projections, where every forward-projection of the intermediate reconstruction is subtracted from the original micrograph prior to its back-projection. Since the reconstruction should have its CTF phases properly flipped, the forward-projection step of SART introduces the CTF (in similar manner as the electron microscope does on the sample) in order to obtain a CTF-affected projection image that is then compared to the original micrograph. In an ideal reconstruction, the forward CTF-affected projection image and the original micrograph are equal. While in simulated images this can be achieved, in real-case tilt-series this is not the case due to the influence of noise.

2.4. SART-specific forward-projection

The SART-specific forward-projection is calculated depending on the tilt angle and the defocus value measured on the corresponding electron micrograph. In principle, the reconstruction is tilted to the specific tilt angle, and subsequently it is shifted up and down in order to accommodate for the measured defocus value. To incorporate the defocus change into the forward-projection, the reconstruction is sliced perpendicular to the beam direction; in principle into slices as thin as the size of one voxel. For each slice of the reconstruction the CTF is applied by phase flipping the negative CTF frequency domains where the defocus is adjusted by the distance of the slice to the center of the reconstruction (Fig. 2). Finally, all phase-flipped slices are summed as in a conventional projection step.

In SART, the forward-projection is calculated from the intermediate reconstruction. In most cases, this primarily contains low-frequency information, as the individual tilt-images do not overlap in Fourier space far enough to cover the high-frequency information. In other words, the current resolution achieved by cryo-electron tomography is far higher than the resolution estimated by the Crowther criterion. Consequently, the back-projected micrographs only overlap at the low frequencies where CTF dampening effects have little influence. It is thus not necessary to introduce a more elaborate CTF application than phase flipping in the forward-projection step, as in the case of Wiener filtering, since it has no influence on the reconstruction quality.

2.5. Back-projection for SART and WBP

Conventional back-projection computes straight rays into the reconstruction. For the 3D CTF correction, the back-projection is carried out slice after slice perpendicular to the beam direction. The difference to conventional WBP is that similarly to forward-projection, the CTF is corrected with the appropriate defocus for every slice depending on its distance from the position where

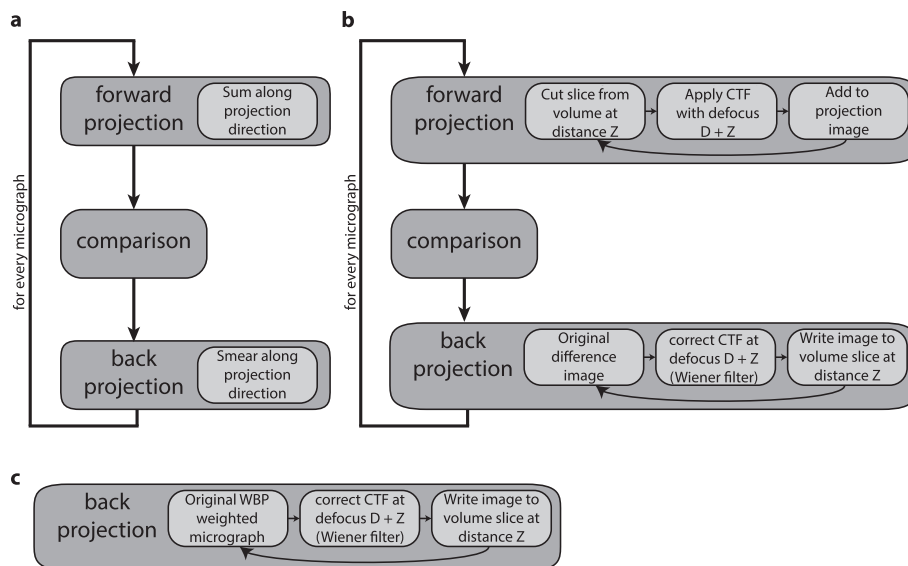


Fig. 3. Comparison of the reconstruction procedure assuming that all micrographs of the tilt-series are aligned. (a) SART reconstruction flow chart without or with 2D CTF correction: For every micrograph, the tilted intermediate reconstruction is forward projected by summing all intensities along the projection direction, which in this case is the beam direction. This so-called “virtual projection” is compared to the original micrograph and the difference image is back-projected into the reconstruction by straight rays. (b) For 3D CTF-corrected SART, the forward-projection is separated into multiple slices, on which the appropriate CTF is applied based on their position in the volume and estimated defocus. Subsequently, all slices are summed, which results in a CTF-affected “virtual projection”. The CTF-affected “virtual projection” is compared to the original micrograph and the difference image is back-projected into the SART reconstruction. However, instead of back-projecting straight rays through the reconstruction, the reconstruction is split into individual slices, and each individual slice is then CTF corrected by Wiener filtering. These slices are then summed up to the intermediate reconstruction. (c) 3D CTF-corrected WBP: Similarly to SART back-projection, the reconstruction is sliced, but instead of the SART difference image, the weighted micrograph is used for back-projection.

the defocus was estimated (Fig. 2). As the original micrograph contains the entire spectral information (including higher frequencies), Wiener filtering is used for back-projection in order to compensate for the oscillations and for the dampening envelope of the CTF during CTF correction. Thus the CTF-corrected image $I_{corrected}$ can be written as:

$$I_{corrected} = \mathcal{F}^{-1} \left\{ \frac{\mathcal{F}\{I_{orig}\} CTF_{model}}{CTF_{model}^2 + p_{noise}} \right\}$$

where \mathcal{F} denotes the Fourier transform, I_{orig} is the original micrograph (for WBP) or the intermediate SART difference image, and CTF_{model} the calculated CTF, based on the defocus measured on the image. We empirically use a constant noise term p_{noise} , set to 0.1, which is related to the signal-to-noise ratio in the image and is similar to previous studies (Chen et al., 2013; Grigorieff, 1998). This ensures that only when signal is present (determined by the empirical threshold of 0.1), it is amplified to compensate the dampening effect of the CTF envelope. A flow chart of the reconstruction process using SART and WBP is outlined in Fig. 3.

2.6. 3D CTF correction: Implementation details

For CTF correction, both the forward- and back-projection images need to be Fourier transformed, which results in a large number of Fourier transforms, in particular, if done voxel precise. On the example of the reconstruction of a tobacco mosaic virus tilt-series, we experience that a slice thickness finer than the precision of the defocus determination for each micrograph is of no practical use, because it only causes the computational costs to increase without improving the resolution. The reconstruction times for WBP with varying slice thickness are shown on Table 1.

Interestingly, it was previously estimated that determining the defocus of an electron micrograph with a precision of better than 100 nm allows for obtaining results after sub-tomogram averaging with sub-nanometer resolution (Schur et al., 2013). Thus, with the 3D CTF correction approach, choosing a slice thickness of several tens of nanometers is a reasonable balance between the computational costs and the resolution of the reconstruction. The resolution after sub-tomogram averaging of the tobacco mosaic virus, as determined by the FSC, shows that the achieved resolution starts worsening with slices thicker than 50 nm, while a 10 nm thick slice gives practically identical results (Fig. 4). Thus the 3D CTF correction does not have to be performed voxel precise, and the computational costs can remain low.

3. Results

We demonstrate the quality gain from the 3D CTF correction using two experiments. Firstly, we use the example of mitoribosomes that was previously published, on which state-of-the-art techniques were applied to extract the most information from the images. The sample was originally reconstructed with weighted back-projection and patch-based CTF correction on the

Table 1
Reconstruction times and achieved resolution depending on the slice thickness used for the CTF reconstruction.

Slice thickness	Reconstruction time, 0× downsampling	Resolution after sub-tomogram averaging
No CTF correction	3:52	n/a
200 nm	4:36	0.88 nm ⁻¹
100 nm	5:34	0.86 nm ⁻¹
50 nm	7:14	0.85 nm ⁻¹
10 nm	19:48	0.85 nm ⁻¹

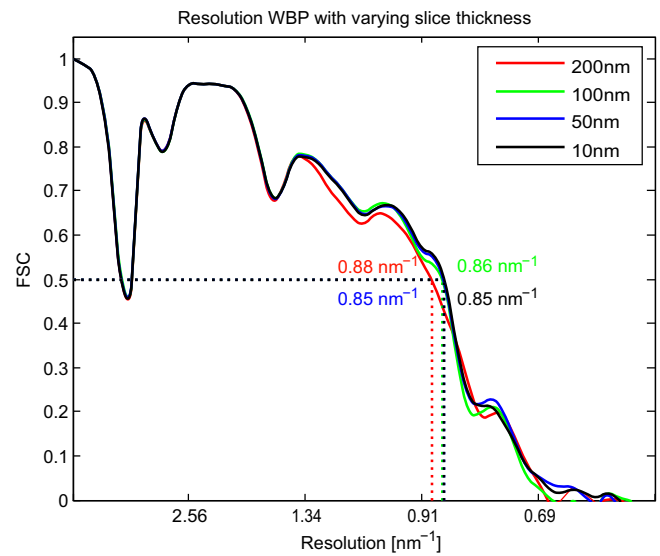


Fig. 4. The achieved resolution depends on the slice thickness during the reconstruction. For this experiment, the defocus for each micrograph was determined with a precision of approximately 50 nm. Choosing a slice thickness less than 50 nm does not improve the resolution. But making the slices too thick worsens the achieved resolution, and finally the same resolution as obtained by conventional 2D CTF correction with phase-flipping of image patches is achieved.

micrographs (Pfeffer et al., 2015a). The second experiment performs a comprehensive comparison between CTF correction with image patches (as performed by IMOD (Xiong et al., 2009)) and the 3D CTF correction. For this experiment, tobacco mosaic virus was used as a standardized specimen and idealized conditions were chosen. In all cases a tomographic reconstruction and sub-tomogram averaging was performed.

3.1. Sub-Tomogram averaging of ribosomes in isolated yeast mitochondria

To guarantee a proper comparison between 3D CTF correction and 2D CTF correction, the exact same values and parameters were used for all steps leading to the reconstruction (Pfeffer et al., 2015a). Altogether, 900 sub-tomograms of membrane-associated ribosomes from 21 tomograms of mitochondria were extracted. For the defocus measurements the values estimated in the original paper were used, which were in good agreement with our own defocus estimates, and ranged from -5 to -7 μm . The cumulative electron dose per tomogram was estimated at 100–120 electrons/ Å^2 . The sub-tomogram averaging was also performed with the same settings, tools and the same masks as used in the original paper resulting into the super-sampling SART 3D CTF-corrected sub-tomogram average (original data: Fig. 5a and d, SART 3D CTF Fig. 5b and e). While the FSC curves are similar, showing a resolution at 2.5 nm^{-1} for 3D CTF correction and 2.8 nm^{-1} for the original data, according to the 0.5 criterion, 3D CTF correction is always slightly better (Fig. 5c and f). Notably, both methods lead to a resolution beyond the first zero crossing of the CTF, which is at approximately 3.2–3.7 nm for a defocus of -5 to -7 μm . In this particular case, while the 3D CTF correction clearly brings immediate improvements, the final resolution is probably not limited by the CTF. The defocus used during acquisition is relatively large which dampens the higher frequencies. Furthermore, the large accumulated total dose plausibly limits the preservation of high resolution information in all micrographs (Dubochet et al., 1988; Grimm et al., 1998).

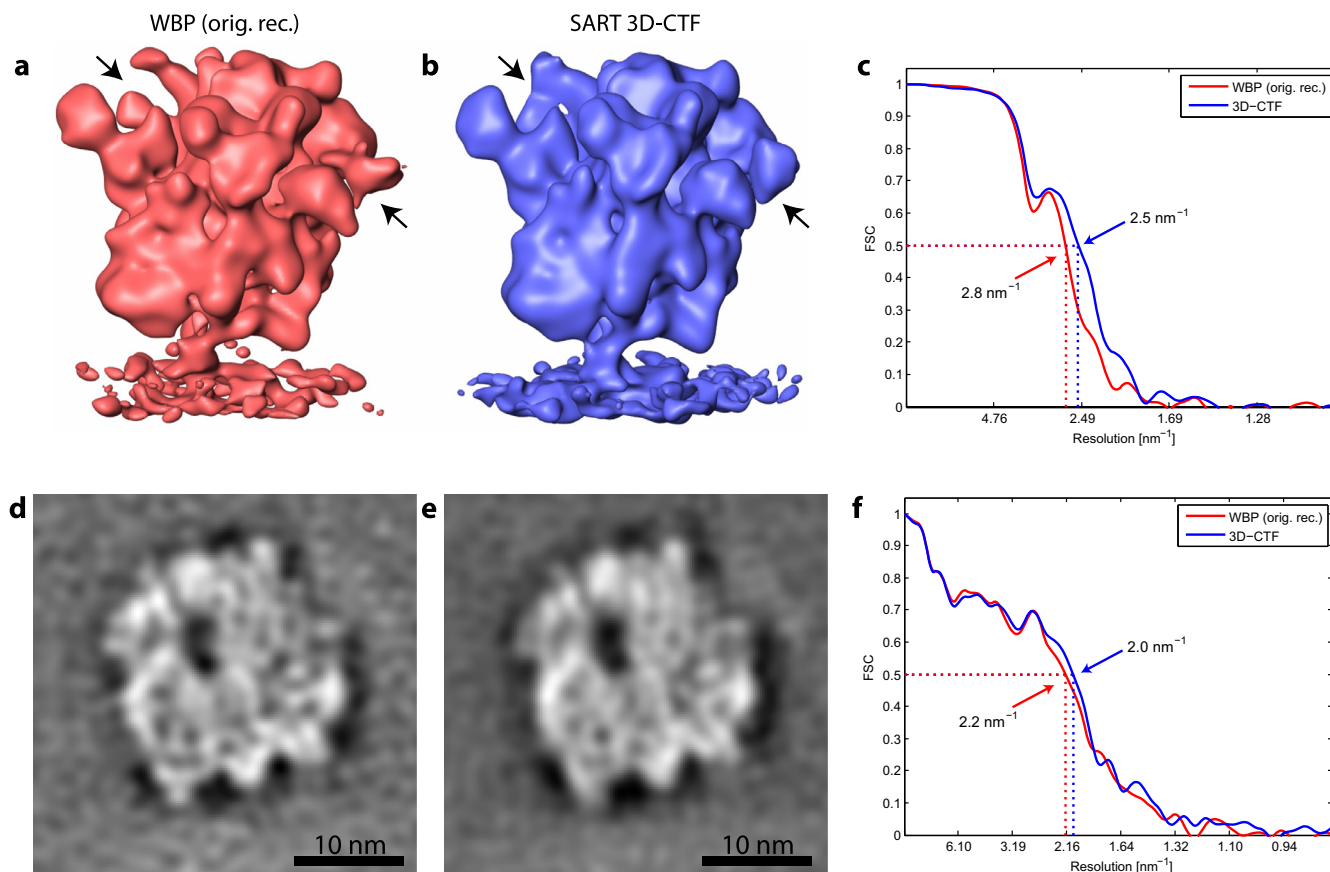


Fig. 5. Mitochondriosomes in isolated yeast mitochondria. (a) Red-colored isosurface of the structure published in Pfeiffer et al. (2015a). (b) Blue-colored isosurface of the sub-tomogram average using 3D CTF correction in combination with super-sampling SART. Arrows point to individual densities missing from the original sub-tomogram average that were recovered after 3D CTF correction. (c) The FSC comparing two half-sets of each average shows a small advantage for the 3D CTF correction, but both structures reveal a similar level of detail. (d) Computational slice through the sub-tomogram average after 2D CTF correction and (e) after 3D CTF-correction. (f) The FSC comparing the reconstructions with the atomic Model 3j6b (Amunts et al., 2014).

3.2. High resolution comparison using tobacco mosaic virus

To explore the performance gain of the 3D CTF correction we recorded tilt-series of TMV in a thicker region of the sample, in which the advantage of sample-thickness-induced defocus correction can display its impact. Thus we used TMVs that were stapled in multiple layers inside the ice with a total thickness of about ~ 150 nm. The tilt-series were then reconstructed with (a) IMOD and patch-based CTF correction, (b) super-sampling SART with 3D CTF correction and (c) standard weighted back-projection with 3D CTF correction. The reconstruction times we obtained for the 3D CTF correction with super-sampling SART and weighted back-projection are shown in Table 2.

For all the reconstructions (IMOD, super-sampling SART, and WBP) the same alignment, and the same processing conditions were used. We further attempted to improve the sub-tomogram average of each individual reconstruction, such as adapting the

CTF-envelope correction, with no significant impact. From the resulting reconstructions, 30,000 sub-tomograms were extracted, and they were subjected to sub-tomogram averaging without constraints, i.e. the helical nature of the sample was not exploited at any time. As a starting reference, the sum of all sub-tomograms was used. To avoid that the resolution would be limited by the electron dose, the final average of each reconstruction method was generated using a reconstruction from a limited range of the tilt-series, using only the first recorded micrographs, such that the total dose was restricted to approximately $34 \text{ e}^-/\text{Å}^2$ as similarly done elsewhere (Pfeiffer et al., 2015b). In the Fourier Shell Correlation curves between each sub-tomogram average and the helical TMV reconstruction (EMBD-1316, (Sachse et al., 2007)), it can be seen that weighted back-projection and super-sampling SART, both with 3D CTF correction, outperform the 2D CTF correction in the complete frequency range, independently of the use of Wiener filtering or just phase flipping (Figs. 6a and 7a). The resolu-

Table 2

Reconstruction times for a tilt-series with 41 micrographs using weighted back-projection and super-sampling SART, both with and without 3D CTF correction. Depending on the GPU, memory restrictions can occur which can be easily overcome by calculating independent sections along the tilt axis. The slice thickness was set to 50 nm and the volume dimension is $3712 \times 3712 \times 600$ voxels. The calculations were performed on a workstation equipped with four Nvidia GeForce Titan graphics cards.

Reconstruction method	Super-sampling	Time in min:s without CTF correction	Time in min:s with 3D CTF correction
Super-sampling SART	1×	6:12	9:04
Super-sampling SART	2×	18:44	33:04
Super-sampling SART	4×	54:14	72:24
WBP	–	3:52	7:14

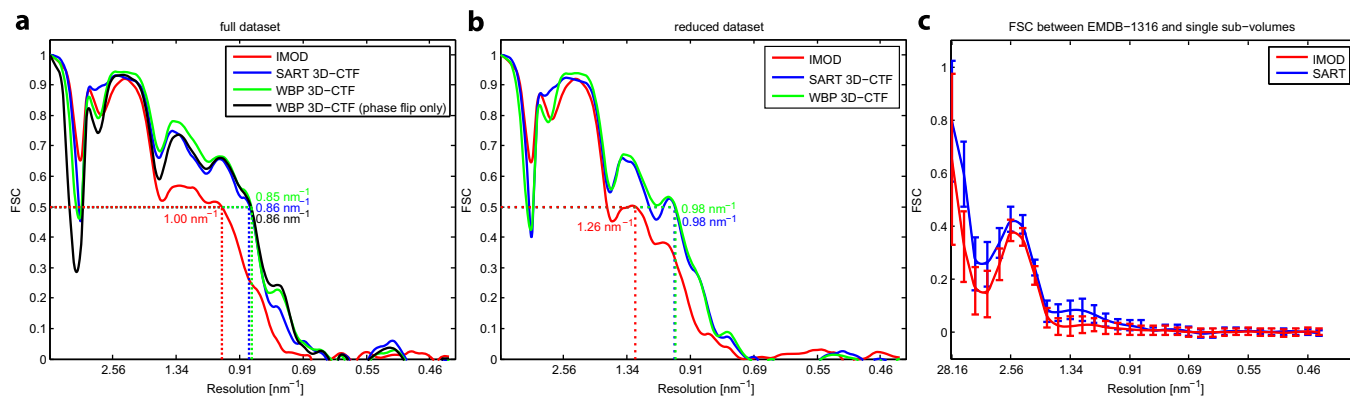


Fig. 6. FSC plots comparing the averages of (a) the full dataset and (b) a reduced dataset with 3625 sub-tomograms. The FSC was always calculated between the sub-tomogram average and the density map obtained by helical reconstruction (EMDB-1316). Whereas 2D CTF correction performed in IMOD (red) never surpasses the one nanometer limit, super-sampling SART (blue), WBP (green) with 3D CTF correction, and WBP (black) with 3D CTF correction and phase flipping only (without the use of Wiener filters), always reach a higher resolution (8.5 Å) using all particles. Using a randomly selected reduced dataset of 3625 sub-tomograms, the SART dataset results in an average comparable in resolution to the average generated with the full dataset using IMOD. (c) FSC comparison of individual sub-tomograms (IMOD (red) and SART (blue)) to the helical reconstruction (EMDB-1316) shows that the signal increase of each individual sub-tomogram increases across the complete frequency range. The error bars show the variance among the 100 FSC curves.

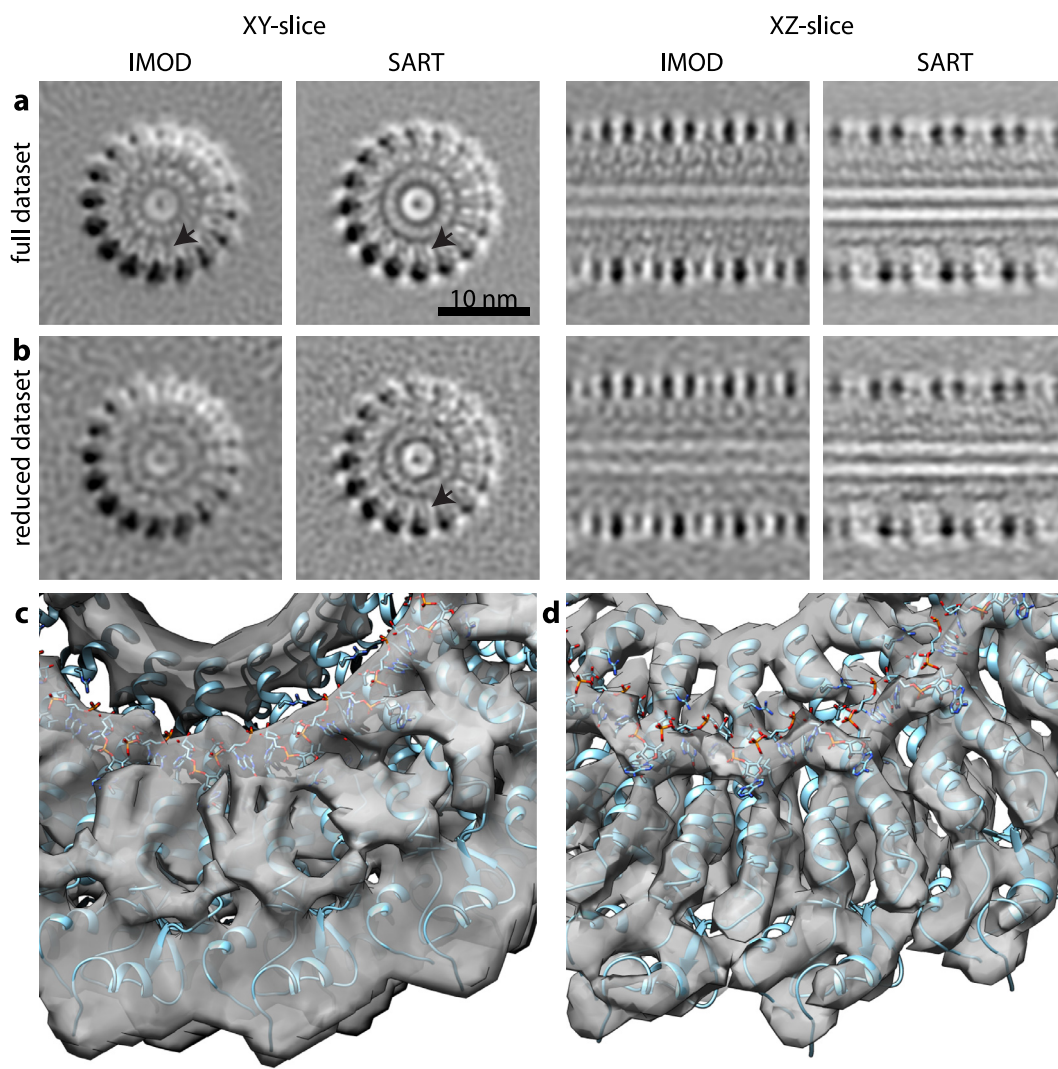


Fig. 7. (a) Orthogonal slices through the sub-tomogram averages reconstructed with IMOD with 2D CTF correction and CTF-corrected super-sampling SART. Apart from the CTF correction, the reconstructions were performed with identical conditions. Arrows point to individual alpha helices. The scale bar is 10 nm. (b) Reduced data set comparison. Where single alpha helices start to be visible in the SART reconstruction with only 3625 particles, the IMOD average only hardly differentiates this sub-nanometer feature with the full dataset. (c) Isosurface of the sub-tomogram average with IMOD (left) and (d) 3D CTF correction with super-sampling SART overlaid with the atomic model from (Sachse et al., 2007) (PDB 2om3). B-factor correction is applied with an amount of -400 \AA^2 .

tion achieved with a reduced data set containing only one eighth of all sub-tomograms (randomly selected from the original set) is comparable to the resolution achieved with 2D CTF correction on the full dataset (Figs. 6b and 7b). Using only approximately 3625 sub-tomograms, a resolution close to 1 nm can be achieved and alpha helices start to be discerned in the slices of the average. When the full dataset is used, 2D CTF correction does not depict secondary structure (Fig. 7c), which in the 3D CTF corrected reconstruction alpha helices become clearly visible in the average and the isosurface density matches well with the atomic model (PDB code 2om3) (Fig. 7d). A visual impression of the reconstructions shows a clear signal gain in the sub-tomogram average from the 3D CTF corrected reconstruction. Furthermore, the sub-tomogram average from the 3D CTF corrected reconstruction shows more contrast with less noise in the background. In fact, the variation of the noise in the background of the 2D CTF corrected sub-tomogram average (Fig. 7c) is comparable to that of the reduced data set sub-tomogram average from the 3D CTF corrected reconstruction.

Even though the resolution of reoccurring structures is improved by sub-tomogram averaging, one of the ultimate goals in tomography remains the recognition of individual events, and individual macromolecular complexes by their structural signature. For this we assessed the gain in resolution on the level of individual (not averaged) sub-tomograms by calculating the FSC between those not averaged sub-tomograms with the density map from the helical reconstruction (EMDB-1316) (Fig. 6c). The plot of 100 FSC curves with the corresponding error bars shows the quality gain in information recovery from this reconstruction technique (Fig. 6c). It can be seen that the FSC curves of the individual sub-tomograms just reach the 0.3 threshold level of the FSC at a resolution of ~ 2 nm, indicating that it should be possible to faithfully recognize individual complexes based on their structural signature for thick samples. This further shows that the signal gain on the level of individual sub-tomograms is much more pronounced, compared to the signal gain achieved after sub-tomogram averaging, potentially because other effects influence the sub-tomogram averaging procedure.

4. Discussion

In cryo-electron tomography 2D CTF correction is the common approach. The micrograph is divided into patches of almost-equal defocus, along the tilt axis of the microscope. Whereas 2D CTF correction takes into account the tilt-induced focus gradient, the sample-thickness-induced focus gradient is neglected. This becomes particularly pronounced at higher tilts when the effective sample thickness increases. Tomography is typically the method of choice when analyzing thick samples, and thus the correction of the sample-thickness-induced focus gradient within the sample is important in order to achieve high resolution reconstructions. Here, we demonstrate the signal gain on a relatively thin sample and a medium thick sample due to the lack of other thicker samples that contain high-resolution information. The reason for this is that most of the thicker samples are recorded at high defocus values, because of the assumption that the achieved resolution is limited. In future, tilt-series of thicker samples could be recorded much closer to focus, thereby allowing the full advantages of this CTF correction method to be explored. Here we would like to mention that in all experiments - also apart from the two presented in this work - 3D CTF correction always produces equal or better results than 2D CTF correction. In some cases we experience that 3D CTF correction does not bring a clear advantage, however, in those cases it is probable that the CTF was not the resolution limiting factor, but rather other issues such as alignment, or radiation

dose or other limitations were responsible. In cases where the conditions were properly controlled, the 3D CTF correction was decisive for an improved resolution.

The Jensen-Kornberg scheme for 3D CTF correction has been introduced a while ago. However a correct and computationally fast procedure was not available until now. Here we have developed a 3D CTF correction scheme that is performed in real space and is only slightly slower than conventional reconstruction methods. The real space implementation provides the advantage that the reconstruction slices can be dealt with sequentially and do not require the Fourier transformation of huge 3D images that renders the reconstruction impractical. Further the CTF correction, while it can also be performed on the CPU, it can be nicely implemented on a modern GPU workstation that delivers a performance that allows for reconstruction times around 1 h for an $8\text{ k} \times 8\text{ k}$ tilt-series using super-sampling SART and only a few minutes for a weighted back-projection reconstruction, and thus it is only slightly slower than conventional reconstruction methods.

We experience that for a proper 3D CTF correction a very precise placement of the reconstruction in the beam is necessary. This is important, because in 3D CTF correction the defocus is corrected along the beam direction, and the individual features should be reconstructed at the defocus value they were actually recorded at. An average estimation of the defocus on the image is not particularly advantageous because individual features such as the carbon film might have a bigger influence on the defocus estimation than biological material. Thus the actual defocus of a specific identifiable feature of which its precise placement in the beam can also be found in the reconstruction must be estimated correctly. From that point on the defocus values of all other features in the reconstruction can be calculated. One suggestion how to do this accurately is to include some carbon in the tilt-series on which both the defocus and its precise 3D placement can be estimated. Ultimately, 3D CTF correction allows for a resolution better than one nanometer and provides additional information in the data at no further experimental cost.

The software will be made available upon request.

Acknowledgements

We would like to thank Friedrich Förster for discussions on the CTF estimation and for the ribosome data. We also thank M. Scheffer for critical reading of the manuscript. This work was motivated by CRC 902 and was supported by an ERC PoC to ASF.

References

- Amunts, A., Brown, A., Bai, X.C., Llacer, J.L., Hussain, T., Emsley, P., Long, F., Murshudov, G., Scheres, S.H., Ramakrishnan, V., 2014. Structure of the yeast mitochondrial large ribosomal subunit. *Science* 343, 1485–1489.
- Bharat, T.A.M., Russo, C.J., Löwe, J., Passmore, L.A., Scheres, S.H.W., 2015. Advances in single-particle electron cryomicroscopy structure determination applied to sub-tomogram averaging. *Structure* 23, 1743–1753.
- Chen, Y., Pfeffer, S., Hrabe, T., Schuller, J.M., Förster, F., 2013. Fast and accurate reference-free alignment of subtomograms. *J. Struct. Biol.* 182, 235–245.
- Dubochet, J., Adrian, M., Chang, J.J., Homo, J.C., Lepault, J., McDowell, A.W., Schultz, P., 1988. Cryo-electron microscopy of vitrified specimens. *Q. Rev. Biophys.* 21, 129–228.
- Erickson, H.P., Klug, A., 1971. Measurement and compensation of defocusing and aberrations by Fourier processing of electron micrographs. *Philos. Trans. R. Soc. London, Ser. B, Biol. Sci.* 261, 105–118.
- Fernández, J.J., Li, S., Crowther, R.A., 2006. CTF determination and correction in electron cryotomography. *Ultramicroscopy* 106, 587–596.
- Grigorieff, N., 1998. Three-dimensional structure of bovine NADH:ubiquinone oxidoreductase (complex I) at 2.2 Å in ice. *J. Mol. Biol.* 277, 1033–1046.
- Grimm, R., Singh, H., Rachel, R., Typke, D., Zillig, W., Baumeister, W., 1998. Electron tomography of ice-embedded prokaryotic cells. *Biophys. J.* 74, 1031–1042.
- Jensen, G.J., Kornberg, R.D., 2000. Defocus-gradient corrected back-projection. *Ultramicroscopy* 84, 57–64.

- Kazantsev, I.G., Klukowska, J., Herman, G.T., Cernetic, L., 2010. Fully three-dimensional defocus-gradient corrected backprojection in cryoelectron microscopy. *Ultramicroscopy* 110, 1128–1142.
- Kunz, M., Frangakis, A.S., 2014. Super-sampling SART with ordered subsets. *J. Struct. Biol.* 188, 107–115.
- Marabini, R., Carragher, B., Chen, S., Chen, J., Cheng, A., Downing, K.H., Frank, J., Grassucci, R.A., Bernard Heymann, J., Jiang, W., Jonic, S., Liao, H.Y., Ludtke, S.J., Patwari, S., Piotrowski, A.L., Quintana, A., Sorzano, C.O.S., Stahlberg, H., Vargas, J., Voss, N.R., Chiu, W., Carazo, J.M., 2015. CTF challenge: result summary. *J. Struct. Biol.* 190, 348–359.
- Pfeffer, S., Woellhaf, M.W., Herrmann, J.M., Förster, F., 2015a. Organization of the mitochondrial translation machinery studied in situ by cryoelectron tomography. *Nature communications* 6, 6019.
- Pfeffer, S., Burbaum, L., Unverdorben, P., Pech, M., Chen, Y., Zimmermann, R., Beckmann, R., Förster, F., 2015b. Structure of the native Sec61 protein-conducting channel. *Nat. Commun.* 6, 8403.
- Sachse, C., Chen, J.Z., Coureux, P.-D., Stroupe, M.E., Fändrich, M., Grigorieff, N., 2007. High-resolution electron microscopy of helical specimens: a fresh look at tobacco mosaic virus. *J. Mol. Biol.* 371, 812–835.
- Schur, F.K.M., Hagen, W.J.H., Marco, A.d., Briggs, J.A.G., 2013. Determination of protein structure at 8.5 Å resolution using cryo-electron tomography and sub-tomogram averaging. *J. Struct. Biol.* 184, 394–400.
- Vargas, J., Otón, J., Marabini, R., Jonic, S., de la Rosa-Trevín, J.M., Carazo, J.M., Sorzano, C.O.S., 2013. FASTDEF: fast defocus and astigmatism estimation for high-throughput transmission electron microscopy. *J. Struct. Biol.* 181, 136–148.
- Voortman, L.M., Stallinga, S., Schoenmakers, R.H.M., van Vliet, L.J., Rieger, B., 2011. A fast algorithm for computing and correcting the CTF for tilted, thick specimens in TEM. *Ultramicroscopy* 111, 1029–1036.
- Wade, R.H., 1992. A brief look at imaging and contrast transfer. *Ultramicroscopy* 46, 145–156.
- Xiong, Q., Morphew, M.K., Schwartz, C.L., Hoenger, A.H., Mastronarde, D.N., 2009. CTF determination and correction for low dose tomographic tilt series. *J. Struct. Biol.* 168, 378–387.
- Zanetti, G., Richey, J.D., Fuller, S.D., Briggs, J.A.G., 2009. Contrast transfer function correction applied to cryo-electron tomography and sub-tomogram averaging. *J. Struct. Biol.* 168, 305–312.